Unraveling the Li Penetration Mechanism in Polycrystalline Solid Electrolytes

Karnpiwat Tantratian, Hanghang Yan, Kevin Ellwood, Elisa T. Harrison,* and Lei Chen*

Lithium dendrite penetration has been widely evidenced in ceramic solid electrolytes (SEs), which are expected to suppress Li dendrite formation due to their ultrahigh elastic modulus. This work aims to reveal the mechanism of Li penetration in polycrystalline SEs through electro-chemo-mechanical phase-field model, using $Li_7La_3Zr_2O_{12}$ (LLZO) as the model material. The results show the Li penetration patterns are influenced by both mechanical and electronic properties of the microstructures, i.e., grain boundaries (GBs). Li nucleates at the GB junctions on the Li/SE interface and propagates along the GB, at which the interfacial compressive stress is small due to the GB softening. Moreover, the excess trapped electrons at the GB may trigger isolated Li nucleation sites, abruptly increasing the Li penetration depth. High-throughput simulations yield a phase map of Li penetration patterns under different trapped electrons concentrations and GB/grain elastic modulus mismatch. The map can quantitatively inform whether the mechanical or electronic properties dominate Li penetration morphologies, providing a strategy for the design of improved SE materials.

1. Introduction

Solid electrolytes (SEs), an alternative to liquid electrolytes, are a potential solution to the utilization of lithium (Li) metal anode.[1] Rechargeable batteries with Li metal anode offer a superior gravimetric energy density when compared to the conventional Li-ion batteries. However, the formation of Li dendrite on the anode's surface, which tends to grow toward the separator, interferes with the cyclability and safety of the Li metal batteries.[2,3] This phenomenon usually occurs when the Li metal anode is paired with the traditional liquid electrolytes,

K. Tantratian, H. Yan, Prof. L. Chen
Department of Mechanical Engineering
University of Michigan-Dearborn
Dearborn, MI 48128-1491, USA
E-mail: leichn@umich.edu
Dr. K. Ellwood, Dr. E. T. Harrison
Research and Innovation Center
Ford Motor Company
Dearborn, MI 48121, USA
E-mail: eharr188@ford.com
H. Yan
State Key Laboratory of Advanced Design and Manufacturing
for Vehicle Body
Hunan University
Changsha 410082, P. R. China

The ORCID identification number(s) for the author(s) of this article can be found under https://doi.org/10.1002/aenm.202003417.

reducing the commercial viability of Li metal batteries. On the contrary, SEs, which are made of ceramics, solid polymer, or their composites, have sufficient stiffness, such that they could be a physical barrier to the Li dendrite propagation, which significantly improves aspects related to safety and performance.[4,5]

Ceramic SEs possess several attractive attributes, including thermal and electrochemical stability, and more importantly high elastic modulus.[1,5] Their elastic moduli could range from tens to hundreds of gigapascals, which are, in theory, more than enough to physically block the growth of Li dendrite penetration.[4,6,7] Unfortunately, Li penetration in such promising ceramic SEs as $Li_7La_3Zr_2O_{12}$ (LLZO) is unexpectedly observed in experimental studies.[8–12] Li filaments are found at microstructural defects such as voids, cracks, and particularly along the grain boundary (GB),[8,13–15] suggesting that the microstructural impact on the Li penetration behavior is significant. Still, the role of microstructure on the suppression of Li dendrite remains unclear.

In a solid-state system, electrochemistry and mechanics are intimately coupled: the volume expansion of the Li metal anode raises the stress variation at the Li/SE interface and this interfacial stress evolution impacts the electrochemical reaction rate. Specifically, during Li plating, the compressive stress, considered as a back stress that opposes the Li dendrite propagation,[16] evolves in the vicinity of newly deposited Li metal.[4,17,18] However, the inhomogeneity of mechanical properties of the SE due to the microstructural defects could lead to a nonuniform stress distribution along the Li/SE interface, potentially triggering Li nuclei on the Li metal surface (**Figure 1**a).[15,17–20] In addition to the mechanical perspective, the excess electrons trapped in defects are recently proposed to be a viable cause of the isolated Li nucleation in the bulk SEs.[21–24] According to the density functional theory studies, the stoichiometric surfaces of cubic and tetragonal LLZO, which represent surfaces of microstructural defects, are electronically conductive.[22,23] The excess electrons can be trapped in these surfaces, lowering the potential in the SE; thus, the reduction of the Li ion in the bulk SE is possible,[21] as illustrated in Figure 1a.

Once nucleated, the propagation and growth behaviors of Li dendrite are dominated by the mechanical properties of the SE, rather than the electronic properties. Li penetrant inside a mechanically hard SE experiences large compressive
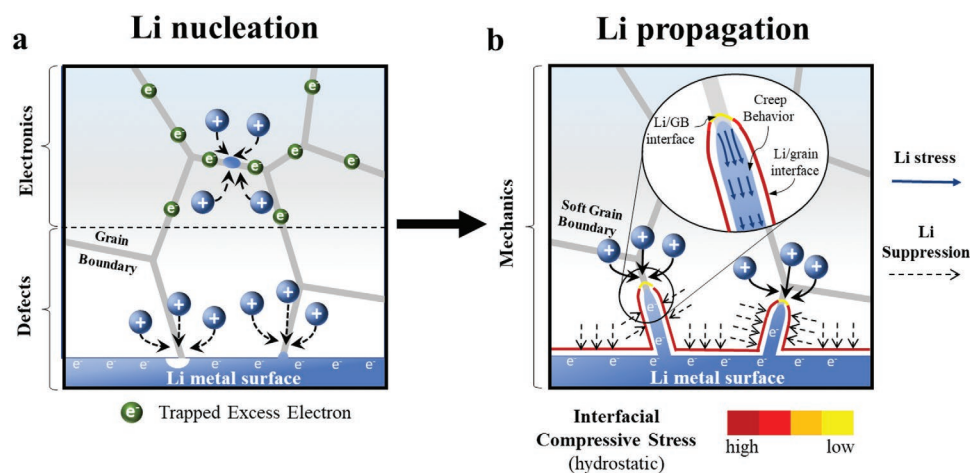
ADVANCED
SCIENCE NEWS
www.advancedsciencenews.com

ADVANCED
ENERGY
MATERIALS
www.advenergymat.de

Figure 1. Schematic illustration of Li nucleation and propagation mechanisms. a) Li nucleation forms at the interface due to the presence of defects, while isolated Li nucleation in the solid electrolyte (SE) is caused by the trapped excess electrons in the grain boundary (GB). b) Li preferentially propagates along the soft GB, at which the interfacial compressive is small, while Li unlikely grows toward the grain interior due to the large interfacial compressive stress.

stress, which exceeds the yield strength of Li. Together with a low melting temperature of Li, at room temperature, Li creep behavior is expected. The creep flow of the deposited Li metal is what controls the interfacial contact between Li metal and SE as well as the interfacial stress generation.[25,26] Herein, we postulate that when the deposited Li metal is in contact with the soft media, such as GBs, the built-up interfacial compressive stress between Li and the GB is small. The small interfacial compressive stress indicates poor mechanical suppression of Li dendrite. Thus, Li preferentially penetrates along the soft GB, and the Li penetrants are likely confined in the GB regions by stiff grain interiors, as shown in Figure 1b. To confirm the above hypothesis, a physic-based theoretical model that explains this complex electro-chemo-mechanical behavior is required.

In this work, we develop the electro-chemo-mechanical phase-field model to unveil the impact of microstructure of SE on the Li penetration behavior. To elucidate how GB softening results in the preferential growth of Li, Li metal deposition in a SE system with a single GB is firstly simulated. The impacts of microstructural architectures and mechanical properties of the GB on the Li penetration behavior are investigated. Moreover, Li penetration in the standard LLZO system is simulated by involving intrinsic mechanical and electronic properties of the SE. Lastly, high-throughput simulations are carried out to draw a phase map of Li morphologies as a function of the GB/grain elastic modulus mismatch and trapped electrons concentration. The map gives quantitative information on how the interplay between mechanical and electronic properties of the GB impacts the Li penetrant morphologies, providing a strategy to engineer the microstructure of SEs to mitigate the Li penetration.

2. Results and Discussion

2.1. The Modified Butler–Volmer Equation

In a SE system, the electrochemical reaction rate not only depends on the activation overpotential, but also the mechanical

stress at the Li/SE interface.[4,15,27–29] From a physical point of view, during Li deposition, the newly deposited Li layer raises the pressure at the interface, which subsequently retards the electrodeposition rate of Li.[15,17,18,30] However, when the deposited Li layer is dissolved, the pressure at the interface is relieved; thus, the impact of mechanical stress is likely diminished. Therefore, we assume that mechanical stress primarily shifts the overpotential of the cathodic reaction. The Butler–Volmer kinetics for Li deposition/dissolution is consequently modified as:

$$I = -I_0 \left\{ \exp\left[\frac{(1-\alpha)F\eta_a}{RT} \right] - c_+ \exp\left[\frac{-\alpha F\eta_a - F\eta_m}{RT} \right] \right\} \tag{1}$$

where $I_0 = ek_0 a_{Li} \gamma_T^{-1}$. Here, $\eta_a = \Delta\varnothing - E^o$ is the activation overpotential and $\eta_m = CP v_{Li}/F$ is the shift of the overpotential due to the mechanical stress,[4,17,29,31] where P and v_{Li} represent the hydrostatic pressure at the interface and molar volume of Li metal, respectively. C is the mechanical overpotential correction factor. The Gibbs free energy along the reaction coordinate is shown in **Figure 2**a. To trigger the electrodeposition process, the negative overpotential ($\eta_a < 0$) is applied so that the energy landscape of <Li$^+$ + e$^-$> is shifted upward, thus the cathodic reaction is dominated. However, the compressive stress ($\eta_m > 0$) moves down the energy landscape of <Li$^+$ + e$^-$>, leading to a decrease of the cathodic current density. The higher the compressive stress at the Li/SE interface, the slower the Li deposition rate becomes.[17] The complete derivation and discussion can be found in Supporting Information.

2.2. Electro-Chemo-Mechanical Phase-Field Modeling

In this electro-chemo-mechanical phase-field modeling, two phase-field parameters (ξ and φ) are introduced to distinct the three-phase system: the Li metal phase ($\xi = 1$, $\varphi = 0$), the GB phase ($\xi = 0$, $\varphi = 1$), and the grain phase ($\xi = 0$, $\varphi = 0$). Each
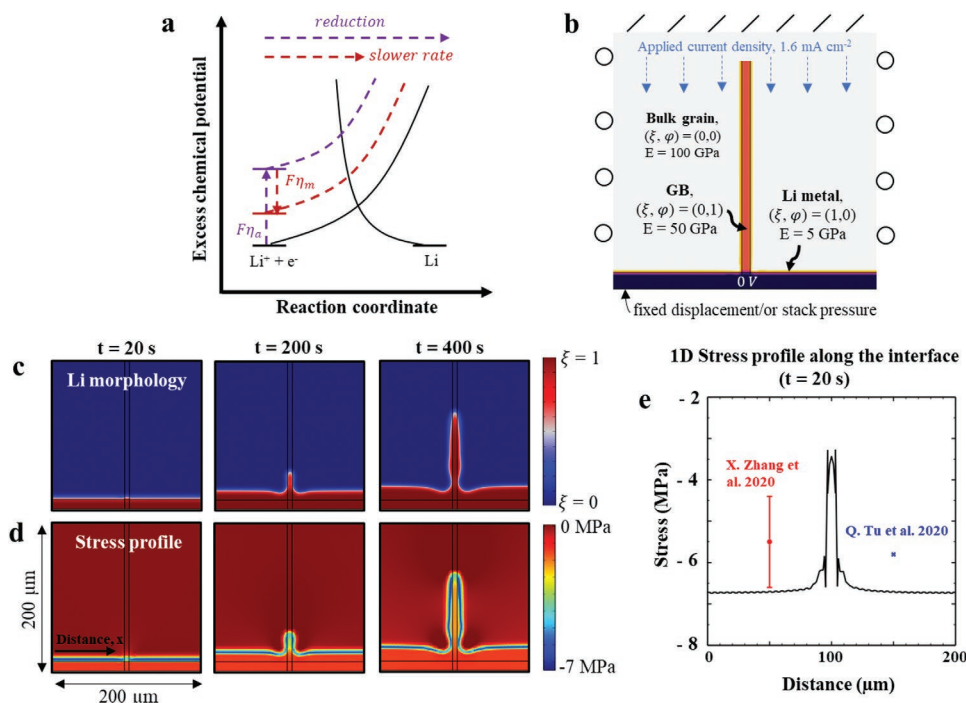
Figure 2. a) The plot of energy barrier along the reaction coordinate for the electrodeposition reaction, $Li^+ + e \leftrightarrows Li$, under the influence of mechanical stress at the interface. b) The geometry, initial and boundary conditions, as well as mechanical properties used in Li deposition simulation. The evolution of c) Li morphology and d) its associated stress distribution under a current density of 1.6 mA cm^{-2}. e) The plot of the resulting stress of Li along the Li/solid electrolyte (SE) interface at the simulation time $t = 20$ s (black) together with the reported maximal interfacial stress in literature, Zhang et al.[26] and Tu et al. [35]

phase-field parameter ranges from 0 to 1. The phase-field equations are expressed as:

$$\frac{\partial \xi}{\partial t} = -L_0\left(g'(\xi) - k\nabla^2\xi\right) -$$
$$L_\eta h'(\xi)\left\{\exp\left[\frac{(1-\alpha)F\eta_a}{RT}\right] - c_+\exp\left[\frac{-\alpha F\eta_a - F\eta_m}{RT}\right]\right\} + \delta_N \quad (2)$$

$$\frac{\partial \varphi}{\partial t} = -L_0^s\frac{\partial F}{\partial \varphi} \quad (3)$$

where L_0 and L_η are constants related to the interfacial mobility and the electrochemical reaction, respectively. δ_N represents the Li dendrite nucleation driving force.[22] Equations 2 and 3 are solved simultaneously with the mass transport (Equation S19, Supporting Information), charge equilibrium (Equation S20, Supporting Information), and the stress equilibrium equation. Stress evolution at the interface involves complicated contact mechanics,[26,32] creep or viscoplastic behavior of Li metal,[25,33] and the volumetric change of the electrode. To make the problem mathematically tractable, we assume that the inelastic strain due to the volume expansion of Li metal is the only source of the internal stress generation, and the contact mechanics is not considered. The stress equilibrium equation is expressed as:

$$\nabla \cdot \boldsymbol{\sigma} = 0 \quad (4)$$

where $\boldsymbol{\sigma} = \mathbf{C}^{eff}\boldsymbol{\varepsilon}^{el}$ and $\boldsymbol{\varepsilon}^{el} = \boldsymbol{\varepsilon} - \boldsymbol{\varepsilon}^0$. $\mathbf{C}^{eff}$ is the effective elastic stiffness tensor. $\boldsymbol{\varepsilon}^{el}$ is the elastic strain wherein small

deformation theory is assumed. The inelastic strain, $\boldsymbol{\varepsilon}^0$, due to the volume expansion of Li metal during the Li deposition process can be expressed as $\boldsymbol{\varepsilon}^0 = \mathbf{K}\,\xi$, where $\mathbf{K}$ is a constant diagonal matrix. $\mathbf{K}$ is obtained by calibrating the resulting stress at the interface to the calculated stress reported in analytical and computational works.[26,34,35] Full description of this electro-chemo-mechanical phase-field model can be found in Supporting Information.

2.3. Influences of GB Softening

Polycrystalline SE contains GBs, which usually have a relatively low elastic modulus,[18,20] compared to the grain interior. Consequently, during the Li deposition process, the built-up of compressive stress at the Li/GB interface is small, resulting in the current focusing and preferential Li deposition in the GB. To clarify this GB softening theory, Li deposition in a SE system with a single GB is simulated. Figure 2b shows the geometry of the simulation domain and the mechanical properties in the system. Note that no artificial nucleation site is employed on the interface. The current density of 1.6 mA cm^{-2}, which is large enough to generate the Li dendrite, is applied to drive the electrodeposition. Moreover, the theoretical studies show the interfacial stress is on the order of a few megapascals.[26,34–36] Thus, through the calibration, the constants related to the inelastic strain are determined to be $K_{ii} = 2.1 \times 10^{-4}$. All simulation parameters are listed in Table S1 (Supporting Information) and more details can be found in Supporting Information.

ADVANCED
SCIENCE NEWS
www.advancedsciencenews.com

ADVANCED
ENERGY
MATERIALS
www.advenergymat.de

The evolution of Li penetrant morphology and stress profile are shown in Figure 2c,d, respectively. Initially, the Li metal surface is perfectly uniform. After applying the current density, the first layer of deposited Li distributes uniformly on the Li metal surface. The Li metal electrode expands equally throughout the Li/SE interface, generating the uniform volumetric strain. However, the GB softening leads to a relatively low compressive stress at the Li/GB interface when compared to the stress at the Li/grain interface. At the simulation time $t = 20$ s, Figure 1e shows that the compressive stress in the GB region is approximately two times lower than the bulk grain region. This results in the acceleration of Li deposition rate in the GB. At the simulation time $t = 200$ s, a small Li penetrant is formed in the GB region as Li continues depositing on the interface, which undergoes a small compressive stress. At the simulation time $t = 400$ s, the formation of Li penetration is fully developed, and the penetration rate increases rigorously at this stage.

Furthermore, the additional investigation on the effects of operating conditions, such as current density and external pressure, on the Li penetration behavior is performed. A larger applied current density leads to a faster Li deposition rate, and thus, a higher Li penetration rate in the GB (Figure S1, Supporting Information). Moreover, a large applied stack pressure essentially adds significant compressive stress throughout the SE system, including the interfacial stress. Thus, the overall Li deposition is reduced. However, the compressive stress at the Li/GB interface is still lower than that at the Li/SE interface due to the softness of the GB; therefore, Li penetration in the GB occurs (Figure S2, Supporting Information).

2.4. Microstructural Dependency

As Li penetrants are formed in the GB region, the microstructure and mechanical properties of GB could play an important role in governing the Li penetration rates and morphologies. In this section, several simulations are performed to illustrate the microstructure architectures and mechanical properties dependency. First, Li deposition behavior in the SE system with various angles between the GB and the Li metal surface is examined. The elastic modulus of the GB and the grain are fixed at 50 and 100 GPa, respectively. **Figure 3**a shows the size of Li penetrant is the largest when the GB boundary direction is perpendicular to the Li/SE interface. The stress at the Li/GB interface is similar for all cases, which indicates a similar mechanical contribution to the reaction rate (Figure 3b). However, the current density (Li deposition rate) decreases with a decrease in angle between the GB and Li/SE interface. This is because Li tends to deposit in the direction of the electric field, which is the main electrodeposition driving force. When the GB is aligned in the same direction to the electric field, the Li penetration rate is the highest.

Next, Li deposition behavior under different elastic moduli of the GB is investigated. Figure 3c indicates that the softer the GB, the larger the size of the Li penetrant. The magnitude of stress at the Li/GB interface decreases with increasing degree of the GB softening. The lower compressive stress leads to the higher current density, as shown in Figure 3d. Obviously,

little to no differences in elastic modulus between the GB and the grain is desirable.

Lastly, the impact of the distancing between each GB on Li penetration rate is studied. The elastic modulus of the GB and the grain are fixed at 50 and 100 GPa, respectively. As the gap between the GBs gets closer, the Li penetration rate decreases, as shown in Figure 3e. Its underlying mechanism can be traced back to the distribution of Li ions (Figure 3f). When the number of Li penetrants in the GB increases, Li ions distribute more uniformly, thus slowing down the Li penetration rate. It is evident in Figure 3g that the Li-ion profile along the cut line at the tips of Li penetrants is more uniform when the gap between the GBs is small. The result implies that polycrystalline SEs with small grain size (or small distancing between GBs) is preferable.

2.5. Intergranular Growth of Li Dendrite in LLZO

In this section, our electro-chemo-mechanical phase-field modeling is applied to simulate the Li dendrite penetration in LLZO by considering both stress and electronic contributions. Measured and calculated properties, including elastic modulus and Li-ion diffusion coefficient of LLZO, are used. The polycrystallin e structure of LLZO is randomly generated with an approximate grain size of 7.5 μm. The elastic modulus of the grain is approximately 158 GPa, while the elastic modulus of the GB is 92 GPa.[20] The calculated trapped electrons concentration in the GB of LLZO is $c_e = 0.337$ mol L^{-1}.[22,23] The current density of 2.0 mA cm^{-2} is applied, which is larger than the reported critical current density in LLZO at room temperature in most literature.[8,13,24,37,38] Other simulation parameters are listed Table S2 (Supporting Information), and the complete details of the initial/boundary conditions can be found in Supporting Information. First, the Li deposition simulation is performed to highlight the growth of Li dendrite penetration under the influence of the GB softening. **Figure 4**a shows the evolution of the intergranular growth of Li dendrite in LLZO, which agrees with the experimental observations.[8] Figure 4b illustrates that the compressive stress at the Li/grain interface is large, resulting in significantly impeded Li deposition into the grain. On the other hand, compressive stress at the Li/GB interface is small, leading to the preferable Li deposition location. The Li morphology is primarily controlled by such an interfacial stress difference induced by the mismatch of the elastic (or plastic) properties between GB and grain. Figure 4c reveals that Li ions are distributed nonuniformly in the SE domain, further promoting the nonuniform Li deposition behavior.

Moreover, to demonstrate the impact of electronic contribution, the trapped electrons concentration is now considered. Figure 4d shows the morphological evolution of the intergranular growth of Li with an additional nucleation site far from the Li/LLZO interface. Theoretically, the Li nucleation probability arises exponentially with increasing excess electrons concentration (Figure 4e). The presence of trapped electrons in the GB (0.337 mol L^{-1}) raises the nucleation probability throughout the GB domain, as illustrated in Figure 4f. Once an isolated Li nucleation site is generated, Li propagates rapidly in the bulk
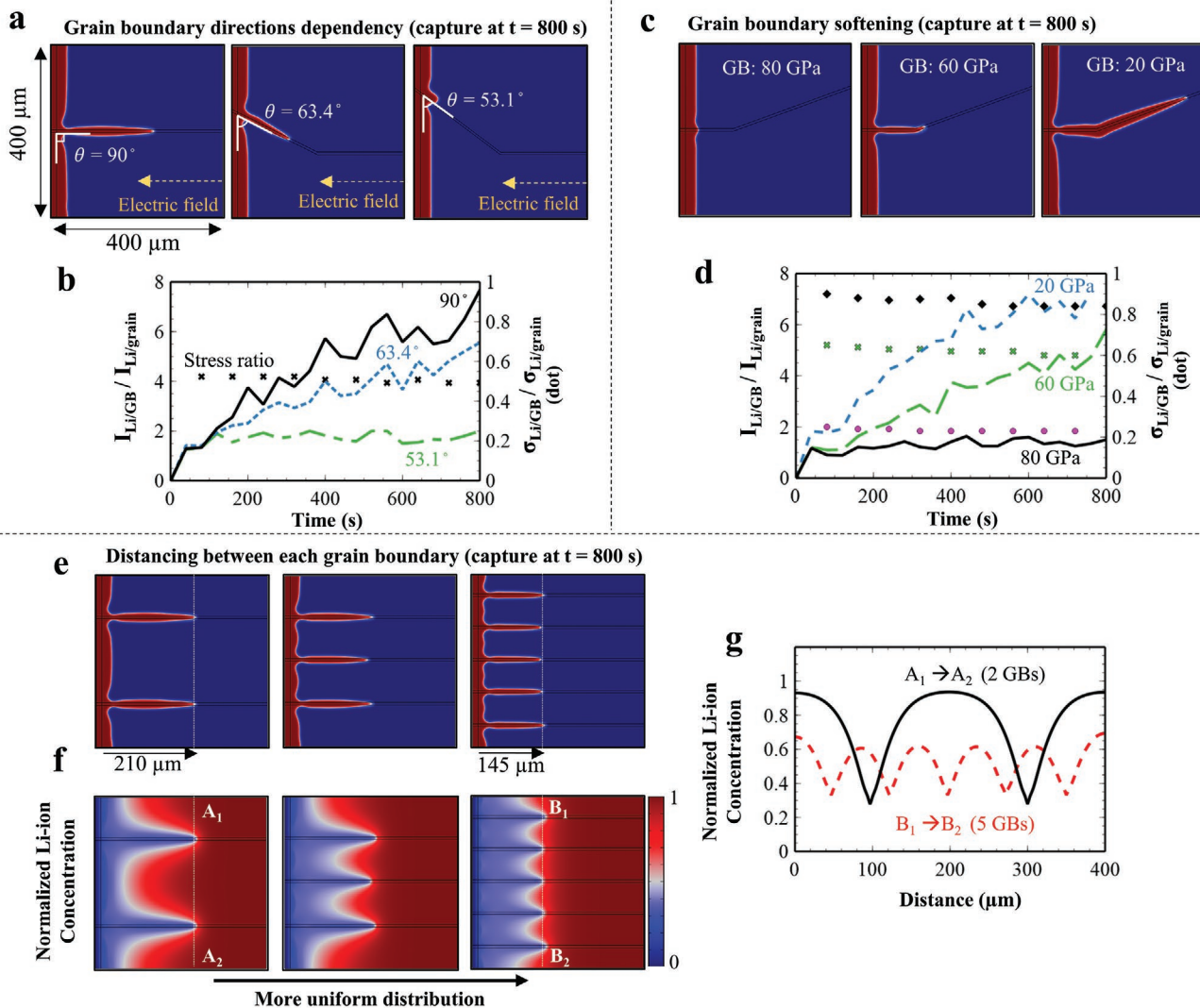
Figure 3. a) Li penetrant morphology in the solid electrolyte (SE) system consisting a single grain boundary (GB) with various angles between the GB and the Li metal surface, captured at time $t = 800$ s. b) The plot of the ratios of (i) the local current density ($I_{Li/GB}/I_{Li/grain}$) and (ii) compressive stress ($\sigma_{Li/GB}/\sigma_{Li/grain}$) at the Li/GB interface to those at the Li/grain interface as a function of time, showing how the alignment of the GB influences the Li penetration rate. c) Li penetrant morphology in the SE system consisting a single GB with different degrees of GB softening, captured at time $t = 800$ s. d) The plot of the ratios of (i) the local current density ($I_{Li/GB}/I_{Li/grain}$) and (ii) compressive stress ($\sigma_{Li/GB}/\sigma_{Li/grain}$) at the Li/GB interface to those at the Li/grain interface as a function of time, illustrating how GB softening impacts the current focusing in the GB. e) Li penetrant morphology and f) Li-ion concentration profile in the SE system consisting multiple GBs with different distancing. g) 1D plot of Li-ion concentration along the cut line $A_1 - A_2$ and $B_1 - B_2$.

SE in all directions along the GBs. The occurrence of the isolated Li nucleation leads to a sharp undesirable rise in Li penetration depth, as shown in Figure 4g.

2.6. Phase Map of Li Morphologies

This section aims to thoroughly investigate how the mechanical and electronic properties of the microstructure in the SE influence the Li penetration behavior. High-throughput simulations of Li deposition are carried out by varying the excess electrons concentration and the elastic modulus of the GB, under a constant applied current density of 2.0 mA cm^{-2}. **Figure 5**

represents the phase map of Li deposition morphologies as a function of the ratio between the elastic modulus of the GB and the grain (E_{GB}/E_{Grain}) as well as the trapped electron concentration. Ideally, the absence of the trapped electrons and the homogeneous mechanical property lead to the uniform Li deposition on the Li metal surface without any sign of Li dendrite (region i). When the GB becomes moderately soft ($E_{GB}/E_{Grain} = 0.8$), Li nucleates at the GB junctions. However, the GB is not soft enough to be a favorable growth path for Li metal; therefore, Li grows in the direction parallel to the electric field, penetrating through the grain interior (region iii). Nonetheless, when the GB is soft ($E_{GB}/E_{Grain} < 0.7$), Li tends to deposit in the GB, forming the intergranular growth of Li dendrite (region ii).
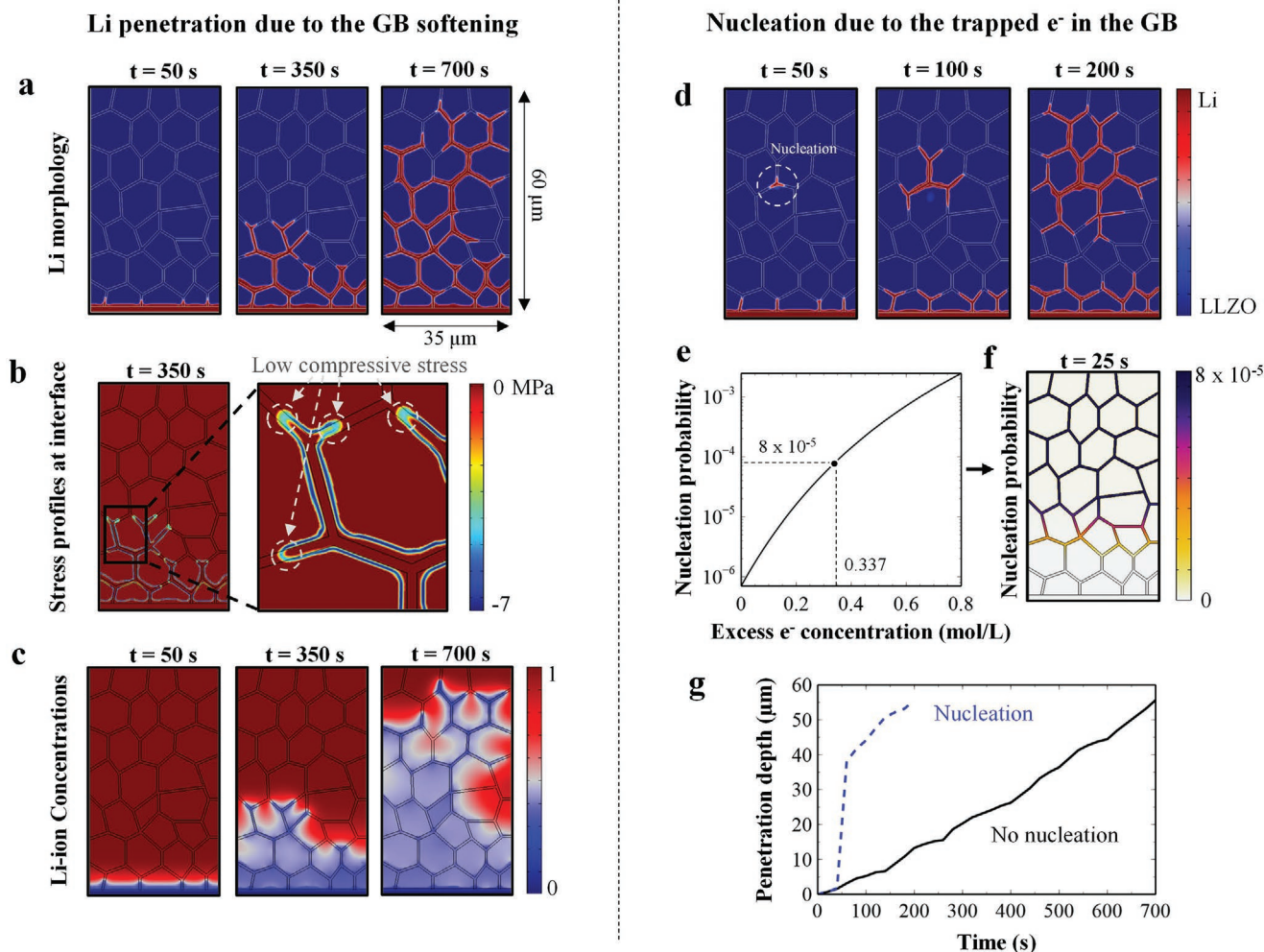
**ADVANCED
SCIENCE NEWS**
www.advancedsciencenews.com

**ADVANCED
ENERGY
MATERIALS**
www.advenergymat.de

Figure 4. a) The evolution of the Li penetrant morphology in polycrystalline LLZO with the elastic modulus of 92 and 158 GPa for the grain boundary (GB) and the grain, respectively. b) The associated stress profile at $t = 350$s, which emphasizes the low compressive stress at the Li/GB interface. c) The evolution of the normalized Li-ion concentration profiles. d) The evolution of Li deposition morphology in the LLZO with the presence of an isolated Li nucleation site due to the trapped electrons concentration. e) The plot of Li nucleation probability against the trapped electron concentration. f) The Li nucleation probability in the GB domain. g) The plot of the Li penetration depth as a function of time for both cases.

These simulation results indicate that the softness of the GB is a primary factor that indicates whether Li preferentially penetrates through the GB or the grain interior.

Furthermore, the increase of the trapped electron concentration in the GB raises the probability of sporadic Li nucleation sites in the SE. The results show the isolated Li nucleation starts to appear when $c_e > 0.15$ mol L^{-1}. However, whether or not the continuous Li deposition on these nucleation sites causes dendrite penetration toward the cathode depends on how soft the GB is. For example, under the condition that the mechanical property of the SE is homogenous, the shape of scattered Li in the bulk SE is spherical, which unlikely leads to the short circuit (region v). However, when the GB becomes slightly softer than the grain, Li deposition likely occurs in the GB regions, forming scatter Li filaments in the bulk SE (region iv). Noticeably, in the bulk SE, Li penetrant is easier to form, compared to the Li filament that grows from the root. This is attributed to the abun-

dance of Li ions (high concentration overpotential) in the bulk SE, which favors the electrodeposition rate. Nevertheless, when the GB is very soft, the rapid Li deposition in the GB tends to connect all Li filaments, forming a large web-like structure of Li dendrite (region ii), which doubtlessly short circuits the batteries. As expressed, the presence of trapped electrons triggers isolated Li nucleation sites. However, the softness of the GB is what dominates the growth behavior of Li dendrite penetration.

Nevertheless, the phase map is generated under a constant current density of 2.0 mA cm^{-2}. If the current density is adjusted, the phase map will change. For example, when the current density is increased (>2.0 mA cm^{-2}), Li morphologies throughout the map will be less uniform. This is because, at a higher applied current density, the current accumulation at the Li perturbation tip is even more concentrated. Consequently, the Li deposition rate at the tip is even faster, leading to a more dendritic shape of Li metal.
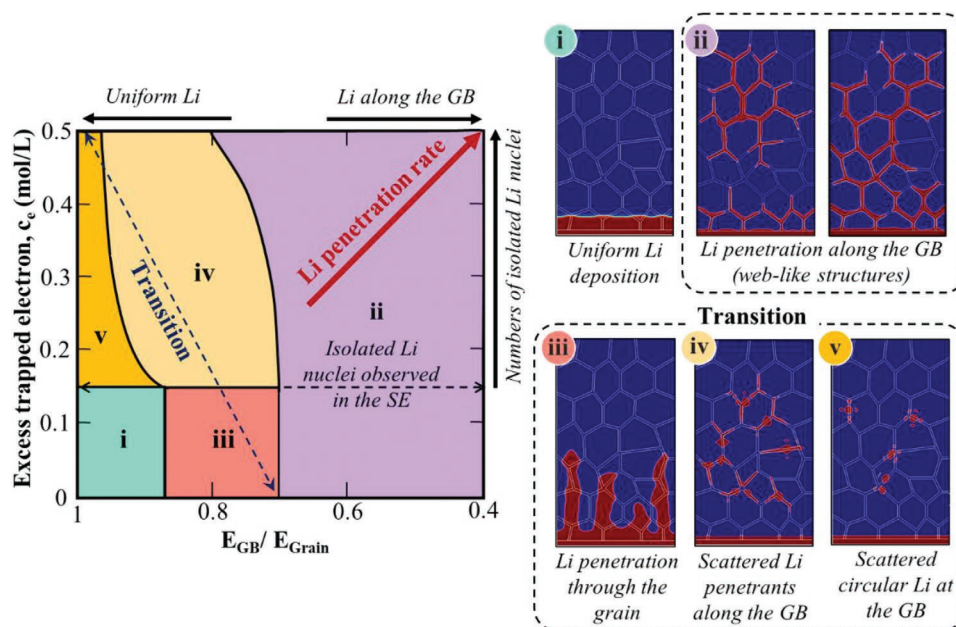
**ADVANCED
SCIENCE NEWS**

www.advancedsciencenews.com

**ADVANCED
ENERGY
MATERIALS**

www.advenergymat.de

Figure 5. The phase map of Li morphologies as a function of elastic modulus mismatch between the grain boundary (GB) and grain (E_{GB}/E_{Grain}) and trapped electrons concentration (c_e) in the GB region under an applied current density of 2.0 mA cm^{-2}. The mechanical action dominates the Li penetration growth behavior, while the trapped electron concentration controls the number of isolated Li nucleation sites in the solid electrolyte (SE).

3. Conclusion

We develop the electro-mechano-chemical phase-field modeling to reveal the Li nucleation and propagation mechanism in polycrystalline SEs. Our results show intrinsic mechanical and electronic properties of the GB play a role in controlling the Li penetration patterns. First, we confirm that the mechanics/microstructure is the driving force behind the Li nucleation and growth on the Li metal surface. The existence of the GB, a soft media, locally leads to a small interfacial compressive at the Li/GB interface during Li depositing. Thus, with the low opposing stress, Li preferentially nucleates and penetrates along the soft GB. In addition, we further demonstrate the impact of the microstructural architectures and mechanical properties of the SEs on the Li penetration behavior. Li penetration rate is the highest when (i) the GB is perpendicular to the Li/SE interface, (ii) the GB is very soft, and (iii) the distancing between each GB is large. Later, we employ our model to simulate the intergranular growth of Li in the famous LLZO by considering the electronic and mechanical properties, estimated by the atomic calculations. Li grows along the GB because of GB softening, and the excess trapped electrons in the GB triggers an isolated Li nucleation in the bulk SE, which critically raises the Li penetration depth. Lastly, we perform high-throughput simulations of Li deposition to draw a phase map that provides quantitative information on how the interplay between mechanical and electronic properties regulates Li deposition morphologies. The map can give an idea of what intrinsic property of the SE might be the primary cause of the observed Li penetration patterns. Hence, further experimental verification can be done feasibly. We hope this fundamental and quantitative understanding of Li penetration mechanism will help facilitate the design of the novel SE materials.

Supporting Information

Supporting Information is available from the Wiley Online Library or from the author.

Conflict of Interest

The authors declare no conflict of interest.

Data Availability Statement

Research data are not shared.

[1] F. Zheng, M. Kotobuki, S. Song, M. O. Lai, L. Lu, *J. Power Sources* **2018**, *389*, 198.

[2] M. Armand, J.-M. Tarascon, *Nature* **2008**, *451*, 652.

[3] T. Ohzuku, *J. Electrochem. Soc.* **2006**, *140*, 2490.

[4] C. Monroe, J. Newman, *J. Electrochem. Soc.* **2005**, *152*, A396.

[5] L. Fan, S. Wei, S. Li, Q. Li, Y. Lu, *Adv. Energy Mater.* **2018**, *8*, 1702657.

[6] F. Zhang, Q. A. Huang, Z. Tang, A. Li, Q. Shao, L. Zhang, X. Li, J. Zhang, *Nano Energy* **2020**, *70*, 104545.

[7] D. Cao, X. Sun, Q. Li, A. Natan, P. Xiang, H. Zhu, *Matter* **2020**, *3*, 57.

[8] E. J. Cheng, A. Sharafi, J. Sakamoto, *Electrochim. Acta* **2017**, *223*, 85.

[9] S. Ozkan, G. Cha, A. Mazare, P. Schmuki, *Nanotechnology* **2018**, *29*, 195402.

[10] E. Kazyak, R. Garcia-Mendez, W. S. LePage, A. Sharafi, A. L. Davis, A. J. Sanchez, K.-H. Chen, C. Haslam, J. Sakamoto, N. P. Dasgupta, *Matter* **2020**, *2*, 1025.

[11] H. Ye, S. Xin, Y. X. Yin, Y. G. Guo, *Adv. Energy Mater.* **2017**, *7*, 1700530.

[12] K. B. Hatzell, X. C. Chen, C. L. Cobb, N. P. Dasgupta, M. B. Dixit, L. E. Marbella, M. T. McDowell, P. P. Mukherjee, A. Verma, V. Viswanathan, A. S. Westover, W. G. Zeier, *ACS Energy Lett.* **2020**, *5*, 922.

[13] L. Porz, T. Swamy, B. W. Sheldon, D. Rettenwander, T. Frömling, H. L. Thaman, S. Berendts, R. Uecker, W. C. Carter, Y. M. Chiang, *Adv. Energy Mater.* **2017**, *7*, 1701003.

[14] A. S. Westover, N. J. Dudney, R. L. Sacci, S. Kalnaus, *ACS Energy Lett.* **2019**, *4*, 651.

[15] G. Bucci, J. Christensen, *J. Power Sources* **2019**, *441*, 227186.

[16] Y. Qi, C. Ban, S. J. Harris, *Joule* **2020**, *4*, 2599.

[17] P. Barai, A. T. Ngo, B. Narayanan, K. Higa, L. A. Curtiss, V. Srinivasan, *J. Electrochem. Soc.* **2020**, *167*, 100537.

[18] P. Barai, K. Higa, A. T. Ngo, L. A. Curtiss, V. Srinivasan, *J. Electrochem. Soc.* **2019**, *166*, A1752.

[19] A. Mistry, P. P. Mukherjee, *J. Electrochem. Soc.* **2020**, *167*, 082510.

[20] S. Yu, D. J. Siegel, *ACS Appl. Mater. Interfaces* **2018**, *10*, 38151.

[21] F. Han, A. S. Westover, J. Yue, X. Fan, F. Wang, M. Chi, D. N. Leonard, N. J. Dudney, H. Wang, C. Wang, *Nat. Energy* **2019**, *4*, 187.

[22] H. K. Tian, Z. Liu, Y. Ji, L. Q. Chen, Y. Qi, *Chem. Mater.* **2019**, *31*, 7351.

[23] H. K. Tian, B. Xu, Y. Qi, *J. Power Sources* **2018**, *392*, 79.

[24] Y. Song, L. Yang, W. Zhao, Z. Wang, Y. Zhao, Z. Wang, Q. Zhao, H. Liu, F. Pan, *Adv. Energy Mater.* **2019**, *9*, 1900671.

[25] Y. Chen, Z. Wang, X. Li, X. Yao, C. Wang, Y. Li, W. Xue, D. Yu, S. Y. Kim, F. Yang, A. Kushima, G. Zhang, H. Huang, N. Wu, Y. W. Mai, J. B. Goodenough, J. Li, *Nature* **2020**, *578*, 251.

[26] X. Zhang, Q. J. Wang, K. L. Harrison, S. A. Roberts, S. J. Harris, *Cell Rep. Phys. Sci.* **2020**, *1*, 100012.

[27] A. Ferrese, J. Newman, *J. Electrochem. Soc.* **2014**, *161*, A1350.

[28] È. M. Gutman, *Mechanochemistry of Solid Surfaces*, World Scientific Publishing, Singapore **1994**.

[29] M. Ganser, F. E. Hildebrand, M. Klinsmann, M. Hanauer, M. Kamlah, R. M. McMeeking, *J. Electrochem. Soc.* **2019**, *166*, H167.

[30] P. Barai, K. Higa, V. Srinivasan, *Phys. Chem. Chem. Phys.* **2017**, *19*, 20493.

[31] S. Sarkar, W. Aquino, *Electrochim. Acta* **2013**, *111*, 814.

[32] P. Wang, W. Qu, W. L. Song, H. Chen, R. Chen, D. Fang, *Adv. Funct. Mater.* **2019**, *29*, 1900950.

[33] W. S. LePage, Y. Chen, E. Kazyak, K.-H. Chen, A. J. Sanchez, A. Poli, E. M. Arruda, M. D. Thouless, N. P. Dasgupta, *J. Electrochem. Soc.* **2019**, *166*, A89.

[34] X. Zhang, Q. Xiang, S. Tang, A. Wang, X. Liu, J. Luo, *Nano Lett.* **2020**, *20*, 2871.

[35] Q. Tu, L. Barroso-Luque, T. Shi, G. Ceder, *Cell Rep. Phys. Sci.* **2020**, *1*, 100106.

[36] A. Verma, H. Kawkami, H. Wada, A. Hirowatari, N. Ikeda, Y. Mizuno, T. Kotaka, K. Aotani, Y. Tabuchi, P. Mukherjee, *Cell Rep. Phys. Sci.* **2021**, *2*, 100301.

[37] A. Sharafi, H. M. Meyer, J. Nanda, J. Wolfenstine, J. Sakamoto, *J. Power Sources* **2016**, *302*, 135.

[38] W. L. Huang, N. Zhao, Z. J. Bi, C. Shi, X. X. Guo, L. Z. Fan, C. W. Nan, *Mater. Today Nano* **2020**, *10*, 100075.